J Mater Sci (2006) 41:4413–4419
DOI 10.1007/s10853-006-0151-3

Aberration-corrected HRTEM of defects in strained La_2CuO_4 thin films grown on $SrTiO_3$

Lothar Houben

Received: 7 February 2006 / Accepted: 21 March 2006 / Published online: 27 June 2006

Abstract The structure of lattice defects in thin La_2CuO_4 films grown under tensile strain on $SrTiO_3$ (001) is investigated by the combination of state-of-the-art medium voltage aberration-corrected transmission electron microscopy together with numerical exit-plane wavefunction reconstruction. The interfacial reconstruction, the coordination in planar shear defects evolving from surface steps and misfit dislocations of the $b = a$[010] type are atomically resolved and analysed. Quantitative mapping and evaluation of peak data related to cation atom columns reveal the formation of a perovskite-like layer of lanthanum copper oxide analogous to the thermodynamically instable $LaCuO_{3-\delta}$ phase and a distortion in the octahedral coordination of copper at the interface to the substrate. The planar shear defects embody extra sites for cations and oxygen in a three-dimensional periodic arrangement which are partially filled and provide paths for vacancy hopping transport. The central structure of the misfit dislocation does not exhibit mirror symmetry around a plane containing the dislocation line owing to the asymmetric arrangement of cation columns.

Introduction

Lanthanum copper oxide represents a system with fundamentally interesting and technically useful properties where the high-temperature superconductivity attained by doping or oxygenation is only the most astounding phenomenon (see e.g. [1, 2] and references therein). Stoichiometric lanthanum cuprate, La_2CuO_4 or La214 in short notation, exhibits a tetragonal to orthorhombic crystal structure transition and alters from a paramagnetic to an antiferromagnetic form as the temperature is lowered. Doping by partial substitution of La with Ba, Sr, or Ca causes the resistivity of the electrically insulating La214 to drop greatly and the material becomes metallic at room temperature. Interstitial oxygen in $La_2CuO_{4+\delta}$ is mobile down to room temperature, allowing for a phase segregation into the antiferromagnetic parent state and a hole-rich superconducting phase [3].

These rewarding properties are foundational for the application of La214 in devices, but can be considerably different in thin films depending on the substrate and on the deposition details. In addition to the structure-wise atomic reconstruction at the strained interface and at lattice defects an ''electronic reconstruction'' [4] near the interface to the substrate is of fundamental interest.

This study employs state-of-the-art techniques in aberration-corrected high-resolution transmission electron microscopy (HRTEM) in order to investigate the interfacial coordination and strain-related defects in nominally stoichiometric thin La214 films grown unbuffered on (001) $SrTiO_3$ (STO). The work focuses on the characterisation of these defects on the atomic scale making use of the recent progress in medium-voltage aberration-corrected high-resolution microscopy towards a quantitative technique for the investigation of lattice defects on the Angstrom scale.

Methodical background and experimental setup

The experimental analyses take advantage from deploying a spherical-aberration-corrected 200 kV instrument together

L. Houben (✉)
Ernst Ruska-Centre for Microscopy and Spectroscopy with Electrons, Institute of Solid State Research, Research Centre Jülich, 52428 Jülich, Germany
e-mail: l.houben@fz-juelich.de

with the numerical retrieval of the exit-plane wavefunction from through-focus series of experimental micrographs. Aberration-corrected images were recorded in a Philips CM 200 FEG ST microscope equipped with a CEOS double-hexapole aberration corrector [5, 6]. With the use of the hexapole corrector the spherical aberration C_S of the instrument becomes a tunable imaging parameter. C_S can therefore be adjusted to balance phase contrast and residual delocalisation while keeping the point resolution close to the information limit of the instrument [6] not within reach during operation of ''traditional'' medium-voltage instruments equipped with a field emission gun. Given a sufficiently thin sample with a thickness just smaller than half the extinction distance favourable conditions for negative phase contrast, i.e. for bright atom contrast, are attained by combining an optimised overfocus with negative spherical aberration [6], i.e.

$$Z_{\text{opt}} = \frac{16/9}{\lambda g_{\max}^2} \quad C_S = -\frac{64/27}{\lambda^3 g_{\max}^4}. \tag{1}$$

At 200 kV accelerating voltage and an information limit $g_{\max}$ of 7.3 nm^{-1}, Eq. 1 delivers Z_{opt}= 13 nm and C_S = −53 μm. The residual delocalisation R for these settings equals 0.08 nm. The resulting ''negative spherical aberration imaging (NCSI)'' [7] conditions were applied in this study to record directly interpretable single high-resolution images. Not only a substantial contrast improvement is achieved hereby but low nuclear-charge elements can also be imaged at bright atom contrast features in the vicinity of high nuclear-charge atoms, which is particularly viable for the investigation of oxide materials [7].

Prior to image recording, Zemlin tableaus were taken from a neighbouring amorphous specimen area and residual wave aberrations were measured and corrected through the alignment of the corrector's hexapole lenses [8]. Wave-aberration corrections up to the 4th order were applied in order to limit the maximum parasitic phase shift at $g_{\max}$ to less than $\pi/4$.

As a complementary method to NCSI imaging, numerical retrieval techniques were applied for the restoration of the phase and the amplitude of the exit-plane wavefunction from a through-focus series using the Philips/Brite Euram software package [9, 10]. The exit-plane wavefunction reconstruction explicitly benefits from the elimination of non-linear imaging artefacts, a reduced low-frequency gap, an improved signal-to-noise-ratio at high spatial frequencies and the possibility for a posteriori measurement and removal of residual parasitic lens aberrations, thus providing essentially delocalisation-free images. Amplitude and phase of the exit-plan wavefunction are therefore excellently suited for the rewarding measurement of the position and the scattering properties of a single atomic column for sufficiently thin samples [11–14].

The La_2CuO_4 films investigated here were prepared by dc-sputtering in oxygen atmosphere of 3.3 mbar on polished $SrTiO_3$ (001) substrates at a heater temperature of 900 °C corresponding to a substrate temperature of approximately 750 °C. Cross-sectional TEM samples were prepared by standard mechanical grinding followed by low-angle (< 10°) Ar^+ ion milling. A final low-energy polishing step at an Ar^+ kinetic energy of 300 eV using liquid nitrogen cooling provided adequately thin samples while containing the amount of surface damage.

For comparison with experimental data images exit-plane wavefunctions were numerically calculated using the EMS image simulation package [15].

Results and discussion

Survey of lattice defects

The nominal lattice mismatch between L214 and STO amounts to $(a_{\text{La214}}-a_{\text{STO}})/a_{\text{STO}} = -2.67\%$ with a_{La214} = 0.38005 nm and a_{STO} = 0.3905 nm, respectively, when neglecting the small orthorhombic distortion of the La_2CuO_4 structure and adopting the pseudo-tetragonal description depicted in Fig. 1. This lattice mismatch with negative sign induces a tensile stress and raises a number of lattice defects.

The La214 layers investigated here maintain a fully epitaxial relationship with the substrate. The c-axis of the La214 is aligned parallel to the [001] substrate normal. With reference to the pseudo-tetragonal La214 lattice, the in-plane orientation relationship $[100]_{\text{La214}} \parallel [100]_{\text{STO}}$ is observed between the film and the substrate.

Figure 2 displays a bright-field image of a La214 film on STO recorded under two-beam conditions close to the [110] zone axis. The diffraction contrast reveals the presence of planar shear defects whose traces are inclined to the substrate normal, similar to those observed by Alimoussa et al. [16]. In most cases, the shear defects start at the interface to the substrate and penetrate the full film thickness. The interface between the La214 and the STO is decorated with closely spaced misfit dislocations that are clearly revealed as dark spots in the image recorded with a g = (004) beam exited. The atomic coordination of both, the planar shear defects and the misfit dislocations will be analysed in the subsequent sections following the analysis of the interfacial coordination.

Interfacial coordination

The interfacial coordination between the La214 and STO determines the electronic properties at the interface.

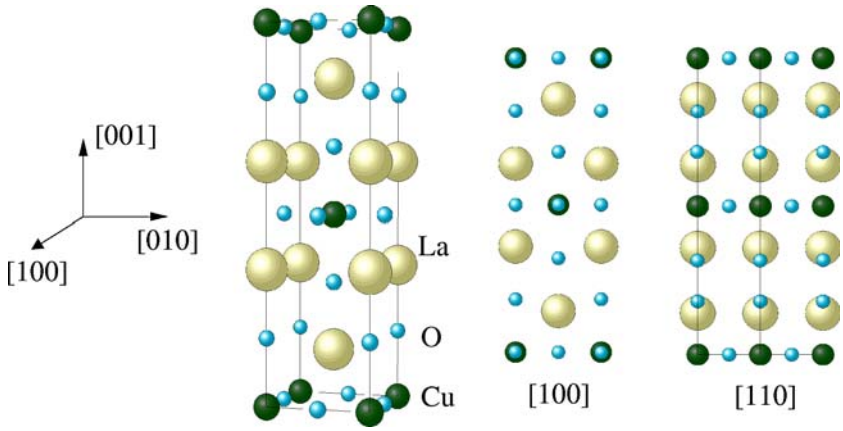

Fig. 1 The pseudo-tetragonal lattice representation for La214. The unit cell vectors of La214 measure a = 0.38005 nm and c = 1.3117 nm. A commendable review of the La214 crystal structure is given in [1]

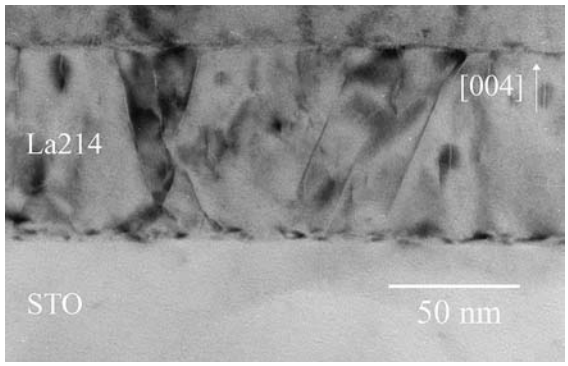

Fig. 2 Diffraction contrast image showing the La214 film grown on top of the STO substrate. The image was taken close to the [110] zone axis under two-beam conditions with the excitation of the g = (004) reflection

Interface-induced electronic reconstructions can, e.g., originate metallic conduction between insulating phases [17]. A detailed examination of the structural reconstruction requires the identification of specific atomic sites. Part of this information can be gained from the directly interpretable aberration-corrected images at minimised delocalisation and from their quantification. In particular, the phase image of the wavefunction retrieved from focal series offers access to the chemistry of an atomic site since the phase is linearly related to the projected potential for sufficiently thin samples. The latter will be used in the following for the determination of the cation lattice structure at the interface.

Figure 3a and b display a NCSI image of the La214/STO interface taken along the [110] lattice direction and a phase image retrieved from a focal series of images taken

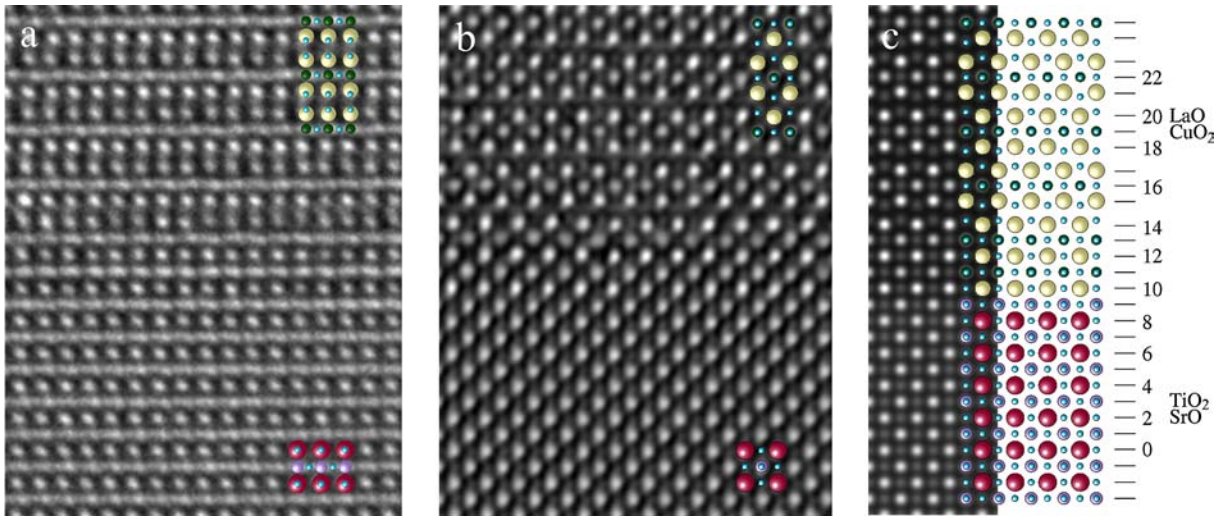

Fig. 3 Atomic structure of the interface between STO and La214. (**a**) NCSI image taken along the [110] viewing direction. (**b**) Phase of the exit-plane wavefunction reconstructed from a focal series of 15 images taken in the [100] zone axis. (**c**) Structure model superimposing the phase image of the simulated exit-plane wavefunction along the [100] viewing direction

along the [100] viewing direction, respectively. Figure 3c shows the phase of the exit-plane wavefunction simulated for the structure model partly superimposed, both of them viewed along the [100] direction. The NCSI image confirms the expected stacking of CuO_2 layers in place of TiO_2 layers and of LaO layers in place of SrO layers in the STO perovskite structure for the first layers grown. In the periodic parts of the experimental phase image of Fig. 3b the La columns appear as the brightest dots, the Sr and the TiO columns appear at a similar phase amplitude and the CuO columns show the weakest peak phase, in agreement with the simulated phase image in Fig. 3c. Quantitative peak phase data for the cation sites in successive layers were evaluated by least-squares regression following procedures described in detail in [14]. The resulting peak data are plotted in Fig. 4a. Instead of the double layers of LaO characteristic for the La214 phase, the interface comprises single LaO layers that sandwich a mixed $(Cu,Ti)O_2$ layer (layers 10–2). On top of these layers the lanthanum copper oxide adopts the K_2NiF_4 structure of the La214 phase.

There are a number of degrees of freedom for the compensation of the electrostatic discontinuity at the polar interfaces between the lanthanum copper oxide and the STO. Assuming that the octahedral coordination of Ti and Cu will be preserved across the interface, the accumulation of electrostatic potential can be avoided by either redistributing electrons, e.g., to the Ti^{4+} site [17] or by the formation of oxygen vacancies or by partial replacement on the cation sublattice, i.e., of La with Sr or Cu with Ti. The experimental results indicate a coexistence of these effects. For example, the mixing of the CuO_2 layer 13 on top of the first LaO layer with Ti helps in avoiding the unfavourable Cu^{3+} state and the following $LaO/CuO_2/LaO$ layer stacking resembles the oxygen deficient perovskite $LaCuO_{3-\delta}$ phase. Furthermore, residual electrostatic forces can be balanced by displacements in the layered interface structure. The plot of the single atom column positions in Fig. 4b reveals that the CuO_2 layer is significantly shifted out of the central position between the LaO layers by about 20 pm. This shift of copper atoms is coincident with the appearance of the buckled LaO double planes and is ascribed to their attractive positive charge overcompensating that of the underlying layers. Because of the multitude of possible structural adaptations as a reaction to the electronic interface formation an interpretation of the local electronic and magnetic properties at the interface remains speculative in this case. Further investigation, e.g., of the crystal field splitting of the e_g and t_{2g} states in the octahedral copper–oxygen coordination is required to evaluate the possible poor metallic or insulating character and weak ferromagnetism that is found in the oxygen deficient $LaCuO_{3-\delta}$ system [18].

Shear defects

The majority of the planar shear defects originates at the interface between La214 and STO. The exemplary NCSI images of such shear defects presented in Fig. 5 were taken along the [110] viewing direction. These shear defects nucleate at steps of the size of a single perovskite block at the La214/STO interface. This can either be a step in the STO substrate or a ''stacking fault'' associated with the lanthanum copper oxide growth, like layer 11 in Fig. 3. Following the interfacial lattice coordination from one to

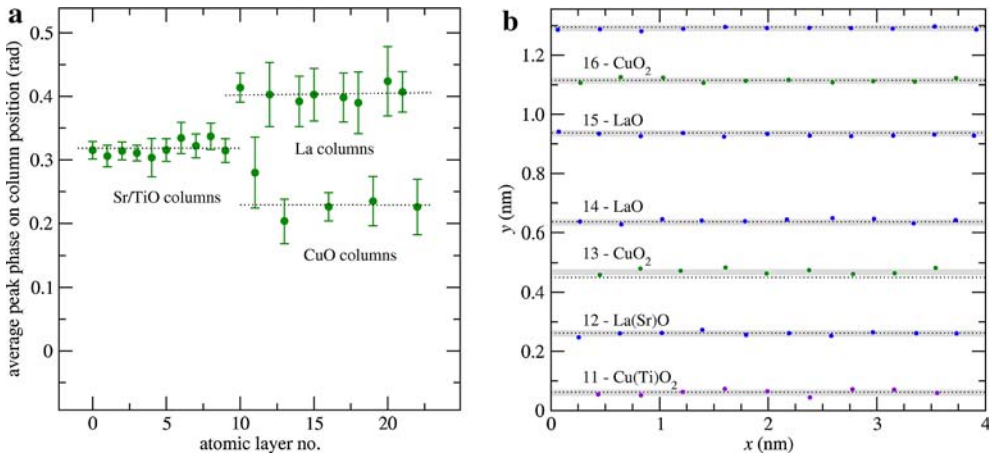

Fig. 4 (**a**) Peak phase data on cation atom column sites in successive layers across the La214/STO interface. A single data point represents the average peak phase for 15 equivalent sites in a monolayer. Each single peak value was evaluated by Gaussian regression to a single phase maximum in Fig. 3b. The error estimates correspond to two times the standard deviation of the 15-point data set. (**b**) Cation column positions at the La214/STO interface. The filled circles mark the phase peak positions measured by Gaussian regression. The grey-shaded regions indicate the extent of the 95% confidence interval for the position of a single column along the interface normal. Dotted lines point out the spacing of lattice planes in the bulk structure

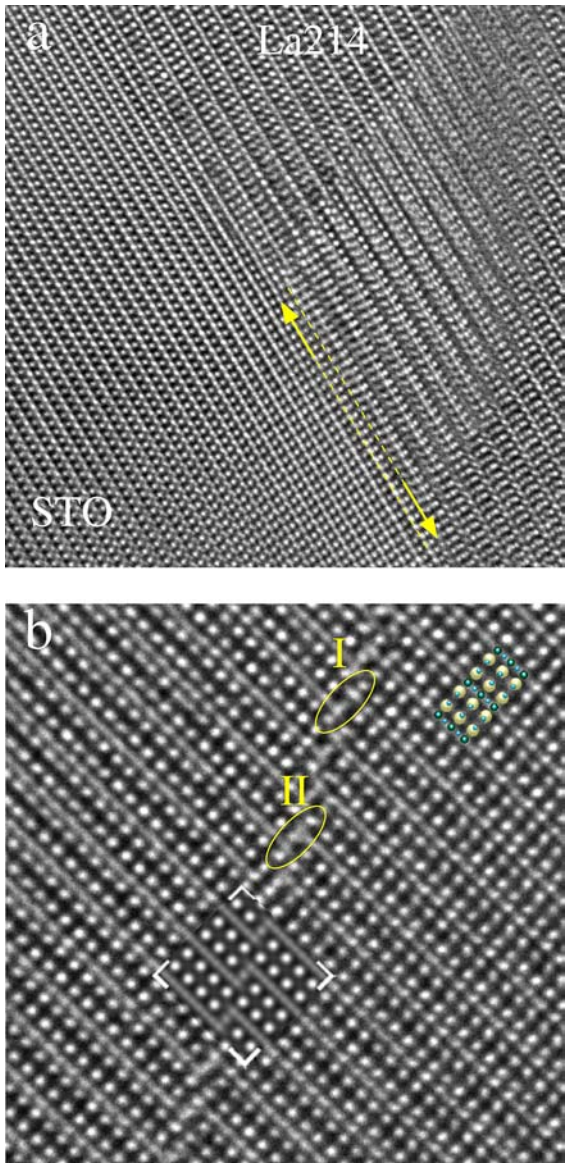

Fig. 5 NCSI images of shear defects originating at the La214/STO interface. (**a**) Shear defect with a habit plane inclined with respect to the [110] viewing direction. The arrows mark the topmost layer of perovskite stacking and highlight an interfacial step of the size of one perovskite block. (**b**) Magnified view of a shear defect. Regions I and II point out a repeating arrangement of five cation columns which is not present in the periodic part. The framed part shows a NCSI image simulated assuming a structure model described in the text

the other side of the shear defect in Fig. 5a this step of a single perovskite block can be clearly observed. The habit plane of the shear defect in Fig. 5a appears inclined with respect to the [110] viewing direction. Obviously, the habit plane is pinned by the direction of the step edge along [100].

Figure 5b shows a magnified view of a shear defect in a thinner specimen region. The two domains are translated in the *c*-axis direction by a quarter of the unit-cell dimension, $\mathbf{R}_{\mathrm{orth}} = 1/4[001]_{\mathrm{La214}}$, corresponding roughly to the height of the interfacial step introducing the defect. Regions I and II mark a particular repeating pattern of five aligned cation columns, which is not found in the periodic structure. The formation of this repeating structure is shown schematically in Fig. 6. Similar structure models were constructed by Galy [19] to propose a mechanism for the formation of over-stoichiometry and under-stoichiometry in $La_{2-x}Sr_xCuO_4$ high-Tc superconductors. We follow the consideration for over-stoichiometry type defects in [19], with the only difference being that those models are based on the assumption that $\mathbf{R}_{\mathrm{orth}} = 1/6[001]_{\mathrm{La214}}$. Figure 6a shows that the copper oxide layers are possibly ended by CuO_5 square pyramids associated with a vacancy site for extra oxygen. In addition, vacant sites for additional cations are formed so that the resulting structure becomes locally over-stoichiometric. Figure 6b shows the next sequence of [110] layers along the viewing direction. The location of the vacancies has shifted with respect to Fig. 6a due to the corrugation of the fault plane on the [100] faces. The superposition of Fig. 6a and b in Fig. 6c brings out the five-cation column pattern highlighted in the experimental image in Fig. 5b. Furthermore, when comparing regions I and II the three inner cation columns exhibit suspiciously different image intensity in agreement with the vacancy character of these sites highlighted in Fig. 6c. In terms of the conductive properties of the grain boundary, it is conceivable that the extra cation and oxygen sites enable ion transport by the hopping of vacancies through the additionally formed boundary sites.

Misfit dislocations

The rigid-body translation associated with the shear defects is a minor contribution to the compensation of the misfit at the interface between La214 and STO. Strain relaxation is achieved by the formation of misfit dislocations. Figure 7 shows the core area of a misfit dislocation by means of the phase image of an exit-plane wavefunction retrieved from a focal series of 15 micrographs. A Burgers circuit drawn around the dislocation core reveals a closure failure $b = a[010]$. Cation atom columns are resolved even in the centre of the dislocation, whereas the image dots associated with oxygen columns gets faint because of the highly strained central part of the dislocation.

The position and amplitude of the dots in the phase image associated with cation columns were determined using a least-squares regression with two-dimensional Gaussian functions following a procedure described in more detail in [14]. Error estimates for the peak positions and amplitudes were calculated making use of the quantification of the Gaussian noise from periodic parts in the phase image [14]. Figure 8 shows a plot of the cation columns' positions in the dislocation core. The 2σ radii for

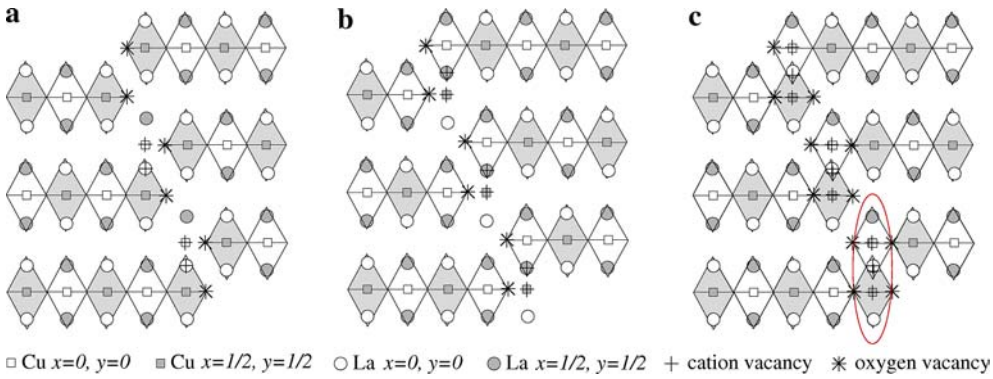

Fig. 6 Detailed drawing of the layer breaking across a shear defect along the [110] viewing direction. The domains are shifted by R = 1/4[001] + 1/2[110]. Additionally introduced cation and oxygen sites may be partially occupied. (**a**, **b**) Structure of the defect in two successive unit-cell layers along the [110] viewing direction. Note the shift by one copper–oxygen octahedron due to the inclination of the habit plane. (**c**) Superposition of (**a**) and (**b**), resulting in the highlighted group of five cation columns observed in Fig. 5b

the unsystematic error of the peak positions are 7–10 pm for columns outside the dislocation centre (smaller than the symbol size in Fig. 8) and 15–20 pm within the centre. The strain field around the dislocation centre is mapped with according accuracy on a sub-unit-cell scale with single cation sites as data points. The interpolation between data points given by the solid lines in Fig. 8. delineates the lattice plane bending associated with the strain field. Where statistical significance better than 95% could be established, elements were assigned according to the peak phase values in comparison with the respective data in the periodic part of the image.

The dislocation centre is located in the first LaO double layer of the La214. At the lower side of the dislocation centre, La occupies Cu sites in the CuO layer, locally forming the double LaO layer typical for the La214 phase, in contrast to the neighbouring area where perovskite stacking prevails. The lattice plane bending around these atomic sites and the slight downward shift of the La column underneath is caused by the larger ionic radius of La compared to Cu. The adjacent Cu column is flanked by an arrangement of double cation columns. The spatial separation between these columns is small in projection meaning that these columns are arranged in a three-dimensional structure and are probably less densely occupied compared to the cation columns in the periodic lattice. The central area of the dislocation slightly deviates from a

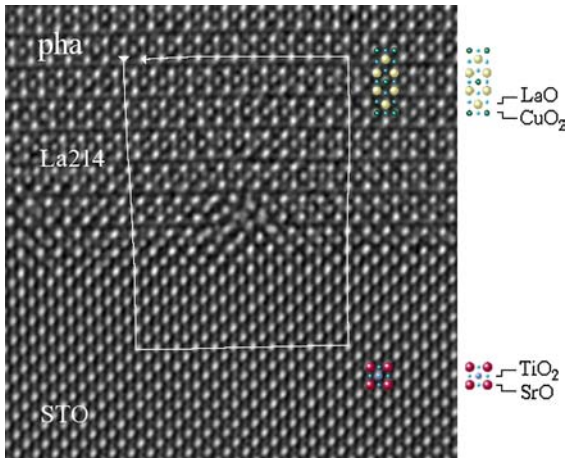

Fig. 7 Misfit dislocation at the interface between La214 and STO viewed along the [100] direction. The image shows the phase of the exit-plane wavefunction. Bright phase peaks are associated with atom columns. Unit-cell projections and a Burgers circuit around the dislocation core are indicated

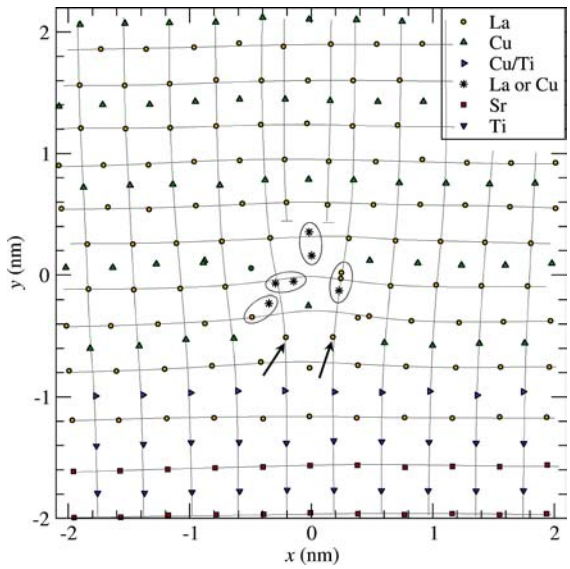

Fig. 8 Cation column positions in the dislocation core. The column positions were determined by least-squares regression to the peak maxima in the phase image displayed in Fig. 7. Elements were assigned according to the peak phase value where meaningful and where statistical significance could be established. Solid lines indicate the lattice plane bending. Closely spaced cation columns in projection are encircled. The arrows mark the occupation of Cu sites by La in the interfacial perovskite-like stacking

mirror symmetry with respect to the inserted lattice planes owing to the asymmetric arrangement of cation double columns.

Conclusions

In summary, negative spherical aberration imaging and numerical restoration of the exit-plane wavefunction from a through-focus series of micrographs have been applied for the investigation of lattice defects in thin films of lanthanum copper oxide at atomic resolution. Directly interpretable contrast features together with a widely minimised image delocalisation enable the proper identification of the structural reconstruction at the interface to the substrate, at internal planar shear defects and misfit dislocations. The quantitative identification of the structural reconstruction, e.g., in terms of vacant sites and single atom column displacements, demonstrates the prospect of success in targeting the evaluation of the electronic reconstruction at such defects on the atomic scale, especially when combining such analyses with complementary analytical work and theoretical calculations.

Acknowledgements The author is grateful to Ulrich Poppe for the preparation of the La214 thin films and for invaluable comments and discussions.

References

1. Pickett WE (1989) Rev Mod Phys 61:433
2. Goodenough JB (2004) Rep Prog Phys 67:1915
3. Jorgensen JD, Dabrowski B, Pei S, Hinks DG, Soderholm L, Morosin B, Schirber JE, Venturi EL, Ginley DS (1988) Phys Rev B 38:11337
4. Okamoto S, Millis AJ (2004) Nature 428:630
5. Haider M, Rose H, Uhlemann S, Schwan E, Kabius B, Urban K (1998) Nature 392:768
6. Lentzen M, Jahnen B, Jia CL, Tillmann K, Urban K (2002) Ultramicroscopy 92:233
7. Jia CL, Lentzen M, Urban K (2003) Science 299:870
8. Uhlemann S, Haider M (1998) Ultramicroscopy 72:109
9. Coene W, Thust A, Op de Beeck M, Van Dyck D (1996) Ultramicroscopy 64:109
10. Thust A, Coene W, Op de Beeck M, Van Dyck D (1996) Ultramicroscopy 64:211
11. Jia CL, Thust A (1999) Phys Rev Lett 82:5052
12. Kisielowski C, Hetherington CJD, Wang YC, Kilaas R, O'Keefe MA, Thust A (2001) Ultramicroscopy 89:243
13. den Dekker AJ, van Aert S, van den Bos A, van Dyck D (2005) Ultramicroscopy 104:83
14. Houben L, Thust A, Urban K (2006) Ultramicroscopy 106:200
15. Stadelmann PA (1987) Ultramicroscopy 21:131
16. Alimoussa A, Casanove M-J, Hutchison JL (1997) Phil Mag A 76:907
17. Ohtomoto A, Muller DA, Grazul JL, Hwang HY (2002) Nature 419:378
18. Bringley JF (1993) Phys Rev B 47:15269
19. Galy J (1992) Acta Cryst B 48:777